Monthly Notices
of the
ROYAL ASTRONOMICAL SOCIETY

Mon. Not. R. Astron. Soc. **416,** 580–590 (2011) doi:10.1111/j.1365-2966.2011.19074.x

Spin-down of protostars through gravitational torques

Min-Kai Lin,[1,2]★ Mark R. Krumholz[1]★ and Kaitlin M. Kratter[3]★

[1]*Department of Astronomy, University of California, Santa Cruz, CA 95064, USA*
[2]*Department of Applied Mathematics and Theoretical Physics, University of Cambridge, Cambridge CB3 0WA*
[3]*Institute for Theory and Computation, Harvard–Smithsonian Center for Astrophysics, 60 Garden Street, Cambridge, MA 02138, USA*

Accepted 2011 May 14. Received 2011 May 14; in original form 2011 February 28

ABSTRACT

Young protostars embedded in circumstellar discs accrete from an angular momentum rich mass reservoir. Without some braking mechanism, all stars should be spinning at or near breakup velocity. In this paper, we perform simulations of the self-gravitational collapse of an isothermal cloud using the ORION adaptive-mesh refinement code and investigate the role that gravitational torques might play in the spin-down of the dense central object. While magnetic effects likely dominate for low-mass stars, high-mass and Population III stars might be less well magnetized. We find that gravitational torques alone prevent the central object from spinning up to more than half of its breakup velocity, because higher rotation rates lead to bar-like deformations that enable efficient angular momentum transfer to the surrounding medium. We also find that the long-term spin evolution of the central object is dictated by the properties of the surrounding disc. In particular, spiral modes with the azimuthal wavenumber $m = 2$ couple more effectively to its spin than the lopsided $m = 1$ mode, which was found to inhibit spin evolution. We suggest that even in the absence of magnetic fields, gravitational torques may provide an upper limit on stellar spin, and that moderately massive circumstellar discs can cause long-term spin-down.

Key words: accretion, accretion discs – hydrodynamics – methods: numerical – stars: protostars – stars: rotation.

1 INTRODUCTION

One of the unsolved problems in the physics of star formation is the spin of protostars (Bodenheimer 1995). The observed specific angular momentum of molecular clouds typically exceeds that of stars by as much as four orders of magnitude (Goodman et al. 1993). Most of the modern attempts at explaining the removal of excess angular momentum from the protostar invoke magnetic torques or magnetic stellar winds (e.g. Matt & Pudritz 2005, 2008; Matt et al. 2010, and references therein). Although some theoretical studies on the effect of purely hydrodynamic star–disc interactions on stellar spin have been carried out (Yuan & Cassen 1985; Popham & Narayan 1991; Bisnovatyi-Kogan 1993; Glatzel & Obach 1999), non-magnetic mechanisms have largely been neglected. However, there may exist situations where magnetic fields are unavailable to remove angular momentum.

Population III stars have long been thought to be unmagnetized due to both the absence of seed fields and the high temperatures required to maintain a sufficient ionization fraction in metal-free gas (Tan & McKee 2004). However, these ideas have recently been challenged (Federrath et al. 2011; Schleicher et al. 2011), and the issue remains unresolved. Recent simulations suggest that without the action of magnetic fields or gravitational torques, the first stars might reach near breakup velocities (Stacy, Bromm & Loeb 2011).

Even for present-day massive star formation, it is unclear whether the magnetic mechanisms normally invoked to regulate stellar spins are applicable. Massive stars form with much higher accretion rates than low-mass ones, and their discs tend to be dominated by gravitational rather than magnetic angular momentum transport mechanisms (Krumholz, Klein & McKee 2007; Kratter, Matzner & Krumholz 2008; Krumholz et al. 2009; Hennebelle et al. 2011; Peters et al. 2011). Naively inserting the high accretion rates typical of massive star formation into the models most commonly adopted to explain T Tauri star spin rates (e.g. Matt & Pudritz 2008) yields the conclusion that massive stars should be spinning at breakup velocity (Rosen, Krumholz & Ramirez-Ruiz, in preparation) , in contrast to observed stellar spins (Wolff et al. 2006). Recent observations of discs around young B stars are also consistent with non-magnetized accretion columns, in contrast to their lower mass counterparts (Eisner et al. 2010). Thus, non-magnetic braking mechanisms are also of interest for limiting stellar spin. Since the most general shape a protostar can have is triaxial, gravitational torques from a protostar acting on its surroundings should be explored.

★E-mail: mkl23@cam.ac.uk (M-KL); krumholz@ucolick.org (MRK); kkratter@cfa.harvard.edu (KMK)

Gravitational torques as an important means of angular momentum transport have been proposed to solve the angular momentum problem of cloud cores in an analytic work by Fisher (2004) and a numerical study by Jappsen & Klessen (2004). However, these authors consider multiple stellar systems. Instead, the simpler problem we consider – that of a single object interacting with its surroundings – is closer to the setup envisioned by Yuan & Cassen (1985). Using existing theories, they discussed how the spin angular momentum of a protostar may be regulated by the circumstellar disc. If the protostar rotates rapidly, it may be subject to instability and become triaxial. It will then exert a torque on the disc, allowing the protostar to transfer angular momentum to the disc. To the best of our knowledge, no numerical simulations similar to Yuan & Cassen's problem have yet been undertaken. However, transport of angular momentum via gravitational torques has been observed in simulations focusing on the first core phase of star formation (Bate 1998; Saigo & Tomisaka 2006; Saigo, Tomisaka & Matsumoto 2008; Saigo & Tomisaka 2011).

In this work, we present calculations of the collapse of an isothermal sphere and study the role of gravitational torques acting on the central object to remove its spin angular momentum. By modelling the central object as a finite-volume fluid body, we demonstrate through simple numerical experiments that its spin can be limited by its deformation and the gravitational interaction with the surrounding medium. In addition, we find that long-term spin-down is possible if the surrounding disc develops $m = 2$ spiral modes, but spin evolution is inhibited if the disc develops significant $m = 1$ non-axisymmetry.

This paper is organized as follows. In Section 2, we describe our model setup and numerical method. We define diagnostic measures in Section 3. We compare and contrast two simulations in Section 4, pointing out important correlations between disc modes and spin-down. We discuss several important caveats to our conclusions in Section 5. In Section 6, we discuss implications of our results on protostellar spins and stellar evolution.

2 STAR–DISC MODEL

We consider the collapse of a cloud leading to the formation of a dense central object surrounded by a disc. For convenience, we will use 'star' and 'stellar' to refer to the central object and its properties, respectively, even though the problem as we set it up is fully dimensionless, so the central object does not necessarily correspond to the physical size or internal structure of a real star. We discuss this issue further in Section 2.2.

The system has mass $M_{\rm sys} = M_{\rm d} + M_*$, where $M_{\rm d}$ and M_* are the disc and stellar masses, respectively. A recent numerical study (Kratter et al. 2010) shows that discs formed via this idealized collapse are characterized by two dimensionless parameters describing its mass accretion and rotation rates.

The accretion of material on to the disc from the cloud is described by the parameter ξ:

$$\xi \equiv \frac{G\dot{M}}{c_{\rm iso}^3}, \tag{1}$$

where $\dot{M}$ is the mass-accretion rate and $c_{\rm iso}$ is the isothermal sound speed. The cloud rotation, responsible for disc formation, is described by the parameter Γ:

$$\Gamma \equiv \frac{\dot{M}}{M_{\rm sys}\Omega_{\rm k}}, \tag{2}$$

where $\Omega_{\rm k}$ is the Keplerian orbital frequency of the material joining the system from the cloud, assumed to occur at the cylindrical radius $R_{\rm k}$ such that $\Omega_{\rm k}^2 = GM_{\rm sys}/R_{\rm k}^3$. It can be shown that

$$R_{\rm k} = \xi^{1/3}\Gamma^{2/3}c_{\rm iso}t = h^2\xi c_{\rm iso}t, \tag{3}$$

where $M_{\rm sys} = \dot{M}t$ has been used, t is the elapsed time and h is the disc aspect ratio at $R_{\rm k}$. In this work, we specify h instead of Γ directly.

The system is modelled as a single, non-magnetic, inviscid and self-gravitating fluid with the density ρ, pressure P, velocity $\boldsymbol{v}$ and gravitational potential Φ. Its evolution is governed by the usual Euler equations and the Poisson equation. To distinguish the central object or star, the pressure is calculated via a barotropic equation of state (EOS)

$$P = c_{\rm iso}^2\rho^{\gamma_1}\left[1 + \left(\frac{\rho}{\rho_*}\right)^{\gamma_2-\gamma_1}\right], \tag{4}$$

where $\gamma_1 = 1.000\,01$, $\gamma_2 = 5/3$ and ρ_* is a fixed transition density defined below.

This EOS mimics star formation by halting gravitational collapse. For $\rho \ll \rho_*$, the fluid collapses isothermally. As the collapse proceeds, the cloud's central density increases. When $\rho \gg \rho_*$, $P \propto \rho^{5/3}$ and further collapse is prevented by the increased pressure. The central object is then effectively a polytrope with the polytropic index $n = 3/2$. Because it has finite volume, it can deform. The resulting non-axisymmetric object may then be spun down due to gravitational torques from the external, lower density disc.

2.1 Initial conditions

The system is initially an isothermal sphere of radius $r_{\rm c}$. For $r \geq r_* \equiv qr_{\rm c}$, where r is the spherical radius and q is a dimensionless parameter, the initial density is

$$\rho_0(r) = \frac{Ac_{\rm iso}^2}{4\pi G r^2}, \quad r \geq r_*. \tag{5}$$

The dimensionless parameter A relates to the accretion rate ξ, and we use tabulated values of A–ξ pairs from Shu (1977). The spherical region $r \leq r_*$ is designated as the initial star. We set $\rho_* = \rho_0(r_*)$ and $\rho_0(r < r_*) = \rho_*$.

The cloud is initialized with an azimuthal velocity

$$v_\phi = 2Ac_{\rm iso}h \times \begin{cases} R/r_* & R \leq r_* \\ 1 & R > r_*, \end{cases} \tag{6}$$

where R is the cylindrical radius. The initial star has solid-body rotation and is below the breakup speed at its equatorial plane but faster than the rest of the core. The latter may bias angular momentum loss from the star to the disc, because if the star becomes triaxial, the pattern speed of the stellar potential felt by the disc may be naturally higher than the disc rotation frequency, exciting trailing spiral density waves in the disc.

Apart from the small region $r \leq qr_{\rm c}$, the initial conditions here are identical to that of Kratter et al. (2010). Our motivation for this setup is the same as in that paper: this setup produces a collapse in which the dimensionless parameters ξ and Γ remain fixed and thus produce a particularly clean numerical experiment for studying the behaviour as a function of ξ and Γ. A real protostellar core, of course, will not follow this simple structure, and ξ and Γ will vary as the core accretes. However, this variation will generally be on time-scales that are long compared to the disc orbital period (e.g. see Kratter et al. 2008; Offner et al. 2010) and we may therefore, to first order, think of the system as simply proceeding through a series

of quasi-equilibrium states with fixed ξ and Γ. Thus, experiments at given ξ and Γ provide valuable insight.

It should be noted, though, that in the idealized collapse described by constant ξ and Γ, the central star is a point mass that can neither gain nor lose angular momentum, whereas in our problem, it can freely exchange angular momentum with the disc. This effect is neglected in simple collapse models, so our cores may evolve away from it. With this in mind, it is best to regard ξ and Γ as initialization parameters.

2.2 Dimensionality and physical scales

As in the self-similar collapse of Shu (1977) and Kratter et al. (2010), the problem we have specified is fully dimensionless, and so we report our results in terms of non-dimensional numbers. In the evolutionary plots shown below, time is scaled by $\tau \equiv 2\pi q(r_c/c_{iso})\sqrt{3/A}$, which is the Keplerian orbital period at $r = qr_c$.

Because our problem is dimensionless, we can scale our simulations to apply to a range of physical systems, in the context of low- and high-mass star formation (and possibly even gaseous planet formation). However, there is one caveat: the dynamic range we are able to achieve in our simulation is much less than the dynamic range involved in the formation of a real star ($r \sim 10^{11}$ cm) from a real protostellar core ($r \sim 10^{17}$ cm). Even with adaptive-mesh refinement, we achieve a dynamic range of $\sim 10^4$, not $\sim 10^6$. If one wishes to scale our dimensionless experiments to physical scales, one may think of doing so in two ways that give a dynamic range comparable to what we achieve.

First, one could envision that we are studying the collapse of a protostellar core leading up to the formation of the first hydrostatic core that is $\sim$5 au in size (Masunaga, Miyama & Inutsuka 1998). Alternatively, one could envision that the size of our central object is the size of a star, but that we are simulating the evolution only of the inner $\sim 10^{15}$ cm of the core that surrounds it. However, there is no evidence that the physical effects we identify depend in the slightest on the dynamic range of the simulations.

2.3 Numerics

The hydrodynamic equations are evolved using the Godunov-type ORION code (Truelove et al. 1998; Klein 1999; Fisher 2002) in Cartesian coordinates (x, y, z). The computational domain is a cube of length $L = 4r_c$. ORION offers adaptive-mesh refinement, a key advantage for the multiscale flow considered here. We do not make use of ORION's sink particle or radiative transfer capabilities in this study. We use a base grid of 128^3 with six levels of refinement, giving the highest effective resolution of 8192^3.

A characteristic length-scale for self-gravitating problems is the Jeans length,

$$\lambda_J = c_s\sqrt{\frac{\pi}{G\rho}}, \tag{7}$$

where $c_s = \sqrt{dP/d\rho}$ is the density-dependent sound speed. For a grid spacing δx, a measure of resolution is $\delta x/\lambda_J$. Our EOS gives

$$\frac{\lambda_J}{\delta x} = \frac{c_{iso}}{\delta x}\sqrt{\frac{\pi}{G\rho}} \times \left[1 + \frac{5}{3}\left(\frac{\rho}{\rho_*}\right)^{2/3}\right]^{1/2}. \tag{8}$$

For example, if $\rho/\rho_* \sim 10$, then the linear resolution is a factor of $\sim$3 better than it would be for gas of the same density obeying an isothermal EOS.

Table 1. Definition of stellar measurements.

Name	Symbol	Definition
Mass	M_*	$\int \rho dV$
Position	$\boldsymbol{x}_*$	$\int \boldsymbol{x}\rho dV/M_*$
Velocity	$\boldsymbol{v}_*$	$\int \boldsymbol{v}\rho dV/M_*$
Rotation radius	S_*	$[\int(\Delta x^2 + \Delta y^2)\rho dV/M_*]^{1/2}$
Orbital angular momentum	j_o	$\boldsymbol{x}_* \wedge \boldsymbol{v}_* \cdot \hat{\boldsymbol{z}}$
Spin angular momentum	j_s	$\int \rho\Delta\boldsymbol{x} \wedge \Delta\boldsymbol{v} \cdot \hat{\boldsymbol{z}} dV/M_*$
Spin frequency	Ω_s	j_s/S_*^2
Breakup frequency	Ω_b	$\sqrt{GM_*/S_*^3}$
KE-to-PE ratio	$T/\lvert W\rvert$	$\int \rho\lvert\Delta\boldsymbol{v}\rvert^2 dV/\lvert\int \rho\Phi dV\rvert$

We use a Jeans number $N_J = 8$ to define the maximum resolvable density

$$\rho_J \equiv \left(\frac{c_{iso}}{N_J\delta x}\sqrt{\frac{\pi}{G}}\right)^2, \tag{9}$$

and we refine if $\rho > \rho_J$ at each grid level. Note the above is the isothermal Jeans density, which is smaller than the true Jeans density based on our EOS. Thus, using ρ_J as defined above is a conservative approach. To ensure the star–disc interface is resolved, we also refine if $\rho > 0.5\rho_*$. We also refine to the highest level within the theoretical disc radius R_k and within one scaleheight in z.

3 DIAGNOSTICS

In this section, we define the diagnostic tools used to interpret our results. Measurements of the star are summarized in Table 1, where integrals are taken over the region $\rho \geq \rho_*$ (dV is the volume element); symbols preceded by Δ are relative to the star; 'KE' and 'PE' stand for kinetic and potential energies, respectively. Note that Φ is the gravitational potential due to all of the fluid.

We regard fluid with $\rho \geq \rho_*$ as stellar. The star has the position and velocity $\boldsymbol{x}_*$ and $\boldsymbol{v}_*$, respectively. The stellar spin angular momentum is defined with the position and velocities of fluid elements with respect to $\boldsymbol{x}_*$ and $\boldsymbol{v}_*$. The stellar rotation radius S_* is defined from its moment of inertia and is used to define stellar spin and breakup frequencies. S_* is not to be confused with the stellar surface where $\rho = \rho_*$, which is typically larger than S_* and generally non-axisymmetric. We use $\langle r_* \rangle$ to denote the average radius in the star's equatorial plane where $\rho = \rho_*$.

The evolution of the star's angular momenta is strongly influenced by the fluid external to the star. The properties of the fluid are measured in cylindrical coordinates (R, ϕ, z) centred on the star with velocities relative to $\boldsymbol{v}_*$. We take the vertical direction of the cylindrical coordinates to be parallel to the vertical (z) direction of the inertial frame, assumed to be aligned with the stellar spin axis. The disc mass M_d is defined to be the difference between the total mass within a cylinder of radius R_k, thickness $2hR_k$, centred about the star, and mass M_*. The disc mass is only defined when the mass within this cylinder exceeds M_*.

For simplicity, we integrate the external fluid vertically over a slab of constant thickness and work with the surface density $\Sigma \equiv \int \rho dz$ and vertically averaged velocity $\boldsymbol{U}$, where

$$\boldsymbol{U} = \frac{1}{\Sigma}\int \rho(\boldsymbol{v} - \boldsymbol{v}_*)\, dz. \tag{10}$$

Our results are insensitive to the extent of vertical integration and in fact also insensitive to whether we use relative velocities or those in the inertial frame.

Non-axisymmetric modes in the surface density of the external fluid can be found via Fourier analysis defined by

$$a_m(R) \equiv \int \Sigma(R,\phi)\exp(-\mathrm{i}m\phi)\,\mathrm{d}\phi, \tag{11}$$

where $a_m(R)$ is the radius-dependent amplitude and m is the azimuthal wavenumber. The integrated amplitude $C_m = \int a_m \mathrm{d}R$ is used as a global measure of mode amplitudes. This integration excludes the star.

The relevant angular momentum fluxes for this problem are

$$F_\mathrm{A} = R\Sigma U_\phi U_R, \tag{12}$$

$$F_\mathrm{R} = R\Sigma \delta U_\phi \delta U_R, \tag{13}$$

$$F_\mathrm{G} = \int \mathrm{d}z \partial_R \Phi \partial_\phi \Phi / 4\pi G, \tag{14}$$

where F_A is the flux associated with large-scale advection, F_R is the flux due to Reynolds stresses and δ here denotes deviations from azimuthally averaged values. F_G is the angular momentum flux associated with self-gravitational torques (Lynden-Bell & Kalnajs 1972). These fluxes can be converted into α viscosities denoted by $\alpha_\mathrm{A}, \alpha_\mathrm{R}$ and α_G, respectively, for example,

$$\alpha_\mathrm{G} = F_\mathrm{G} \Bigg/ \left\langle R \left| \frac{\mathrm{d}\ln\Omega}{\mathrm{d}\ln R} \right| \Sigma c_\mathrm{iso}^2 \right\rangle_\phi, \tag{15}$$

and similarly for α_A and α_R. $\Omega \equiv U_\phi/R$ is the angular velocity and $\langle\,\cdot\,\rangle_\phi$ denotes an azimuthal average.

It is important to regard the α viscosities above simply as non-dimensionalized fluxes rather than the viscosity coefficient in accretion disc models (Shakura & Sunyaev 1973, which would impose $0 \le \alpha \lesssim 1$). A positive flux out of the star indicates spin angular momentum loss. To ensure that this angular momentum loss is physical rather than numerical (since ORION does not exactly conserve angular momentum), we can compare the physical α viscosities we measure with the effective numerical viscosity, denoted by α_N, measured for the ORION code by Krumholz, McKee & Klein (2004).

It will also be useful to consider mass-accretion rates. To measure the ξ parameter from our simulations, we define

$$\xi_\mathrm{sim} \equiv \frac{G}{c_\mathrm{iso}^3}\frac{\mathrm{d}}{\mathrm{d}t}(M_* + M_\mathrm{d}). \tag{16}$$

Although this is the most natural definition, because frequent simulation output is not practical due to the large data sizes involved, the numerical time-derivative only gives an estimate. Nevertheless, we find that the mass-accretion rate is consistent with the behaviour of stellar spin.

4 RESULTS

We study the evolution of the star's spin in two cases. In Case 1, we consider initial conditions leading to a large disc-to-star mass ratio. For our comparison (Case 2) run, we consider initial conditions which lead to a smaller disc-to-star mass ratio. We shall see that on the overall simulated time-scale, the massive disc (Case 1) is less efficient at spinning down the star than its lower mass counterpart (Case 2) due to different azimuthal spiral modes dominating the angular momentum transport.

Before discussing our two cases, we should mention an important constraint on our parameter choices. Kratter et al. (2010) have established the ranges in parameter space for which disc fragmentation is or is not expected. We limit ourselves to values of ξ and Γ such that the disc will be non-fragmenting within the simulation. We do so in order to render the numerical experiment as clean and easy to interpret as possible.

Massive stars form with high accretion rates that do tend to produce gravitationally-unstable, fragmenting discs (Kratter & Matzner 2006; Krumholz et al. 2007, 2009; Kratter et al. 2008; Peters et al. 2010; Hennebelle et al. 2011). However, protostellar discs are heated by the central star and by viscous dissipation, both of which increase at smaller radii, so that fragmentation generally occurs only outside $\sim$100 au. Since it is the angular momentum flux out of the star to the disc that counts, it is the inner disc that is important for star–disc angular momentum exchange. This means that our choice to limit ourselves to the non-fragmenting part of parameter space does not prevent us from applying our models to massive protostars and their discs.

4.1 Case 1

This case has parameters $\xi = 5.58$ ($A = 4.0$), $h = 0.1$ and $q = 0.005$. We start measurements after the star is sufficiently resolved at the finest grid level. The radius $\langle r_* \rangle$ is typically resolved by at least 20 cells.

4.1.1 Self-limited spin-up

We first describe the early evolution $4 \le t \le 11$, when the disc mass is insignificant compared to the stellar mass. Figs 1 and 2 show snapshots of the density field and the evolution of stellar properties, respectively.

At $t \lesssim 6.2$, the star spins up with a rapid increase in j_s, $\Omega_\mathrm{s}/\Omega_\mathrm{b}$ and $T/|W|$ as it accretes material and angular momentum. Because $\Omega_\mathrm{s} = j_\mathrm{s}/S_*^2$, spin-up can occur because of decreasing S_*, but our EOS inhibits further collapse when $\rho \gg \rho_*$. Hence, the spin-up is due to accretion, as expected for initial collapse. As it spins up, the star deforms into a bar-like object (Fig. 1, $t = 6.66$). The bar-shaped star exerts a positive gravitational torque on the surrounding material because it spins faster than the surrounding material, producing spiral arms in the latter (Fig. 1, $t = 7.23$). This counteracts the increase in stellar spin angular momentum due to the accretion of material, resulting in an approximately constant j_s during $6.2 \lesssim t \lesssim 7.7$.

From $t = 8$–10, spiral arms are always present in the external fluid (e.g. Fig. 1, $t = 9.25$) and Fig. 2 shows that j_s is decreasing during this time-interval. This indicates spin angular momentum loss due to the negative torque exerted on the star by the prominent spiral arms. Thus, the initial spin-up is limited by the increasing spin-down torque from the external fluid as the star becomes deformed into a non-axisymmetric, $m = 2$ object. Note in Fig. 2 that $|j_\mathrm{o}| \ll |j_\mathrm{s}|$ so the star is essentially fixed in the x–y plane in the inertial frame. However, note that the increase in j_o at $t = 9.4$ coincides with when j_s and $\Omega_\mathrm{s}/\Omega_\mathrm{b}$ stop decreasing. This suggests that orbital motion hinders spin-down.

Fig. 3 compares the angular momentum fluxes at $t = 9.25$, when j_s is decreasing.[1] The rise in gravity flux towards the average stellar surface, to $\alpha_\mathrm{G} \sim 0.5$ at $\langle r_* \rangle$, implies some angular momentum loss due to gravitational torques. The figure shows that $\alpha_\mathrm{A} < 0$ around $\langle r_* \rangle$ which indicates that large-scale advection is spinning up the

[1] Defining the external fluid relative to the star implies an indirect potential associated with stellar motion, but this vanishes when performing azimuthal averages.

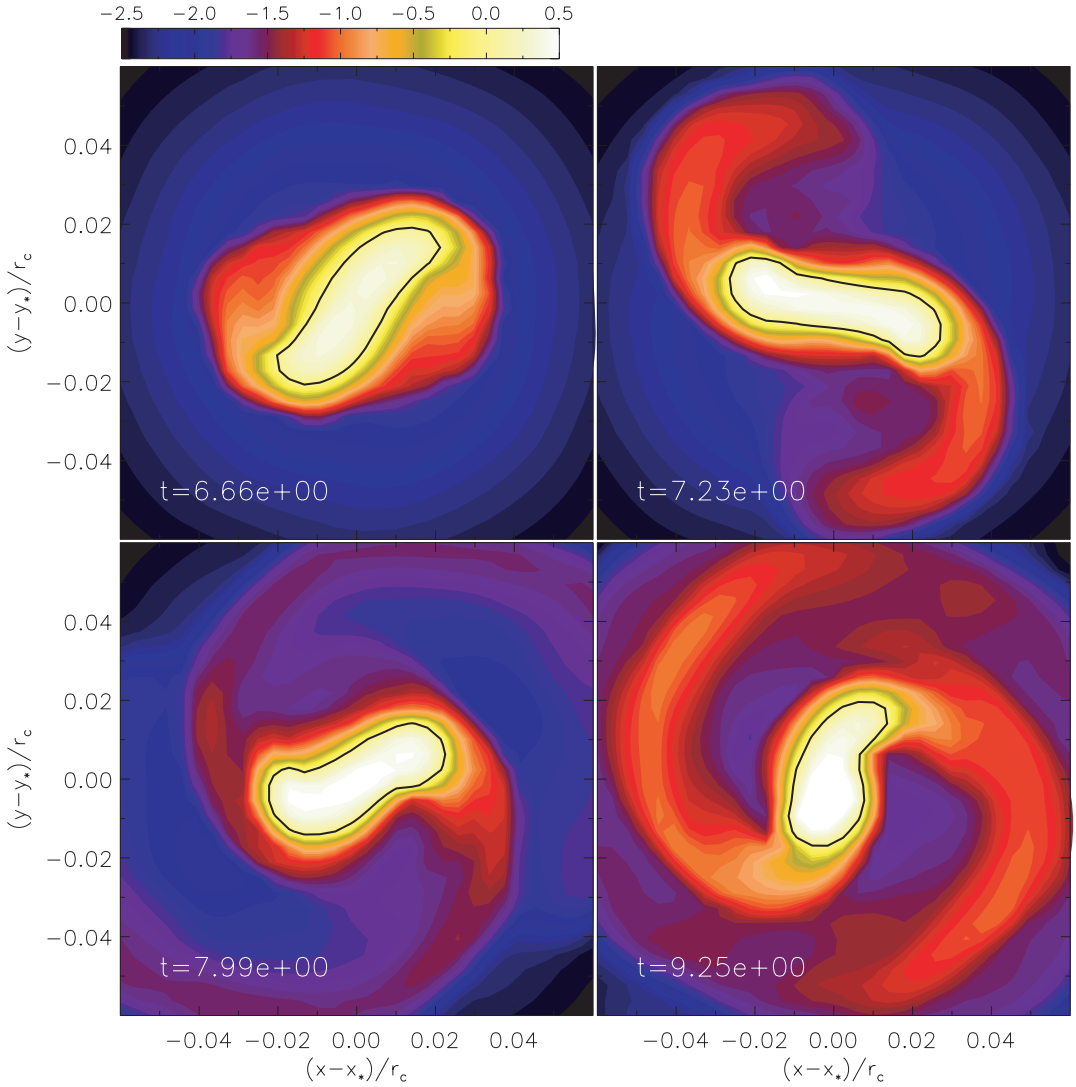

Figure 1. Case 1: contours of $\log(\rho/\rho_*)$ in the star's equatorial plane at four snapshots during the initial collapse. Thick lines delineate $\rho = \rho_*$.

star, but $\alpha_G + \alpha_A \sim 0.2 > 0$, implying that gravitational spin-down torques outweigh the effect of accretion, thereby preventing spin-up and leading to spin-down. The numerical viscosity is estimated to be $\alpha_N \sim 0.03$ near $\rho \simeq \rho_*$ and is therefore negligible.

We also explicitly solve for the gravitational potential Φ_* associated with $\rho > \rho_*$ and find a positive torque exerted by the star on the external fluid, as shown in Fig. 4. This torque is concentrated near $\langle r_* \rangle$. Together with the contour plots in Fig. 2, this is consistent with prominent $m = 2$ spirals in the density field being responsible for spinning down the star.

4.1.2 Long-term evolution

We ran Case 1 until the stellar spin approached a steady state. Its evolution is summarized in Fig. 5. Note that the early phase discussed previously, when most variation in stellar spin occurs, coincides with the time when the predicted disc is undefined.

Between $11 \lesssim t \lesssim 26$, Ω_s/Ω_b is highly variable but settles to $\simeq 0.5$ at $t = 34$. Between $39 \lesssim t \lesssim 74$, it decreases at a negligible rate compared to $7.7 \lesssim t \lesssim 11$. Most of the variation in $T/|W|$ also diminishes after $t = 26$. Note that Ω_s/Ω_b and $T/|W|$ become relatively constant as M_d/M_* increases.

The stellar spin angular momentum behaves similarly. There is no appreciable change in j_s relative to $t \lesssim 11$ after disc formation. However, between $11 \lesssim t \lesssim 20$, the orbital angular momentum increases by two orders of magnitude (comparing j_o in Figs 2 and 5) from essentially zero to values comparable to j_s: at $t \simeq 20$, $j_o \simeq 0.056$ and $j_s \simeq 0.011$.

As M_d/M_* increases from ∼0.3 to ∼0.5, the orbital angular momentum j_o undergoes large oscillations, which are comparable in magnitude to j_s. Indeed, we found that the star exhibits complex orbital motion, and its displacement from the box centre can be $\sim 0.022 r_c$, larger than its size ($\langle r_* \rangle \simeq 0.0146 r_c$). Significant orbital motion coincides with disc formation.

The evolutionary plots suggest that the disc inhibits changes to stellar spin. Instead, its interaction with the disc leads to orbital motion. This is consistent with a Fourier analysis of the surface density shown in Fig. 6.[2] During the self-limited spin-up phase ($t < 11$), the $m = 2$ mode is dominant in the external medium to the

[2] As the predicted disc does not develop until $t \simeq 20$, strictly speaking, amplitudes prior to this time are not disc modes but simply that of the external medium.

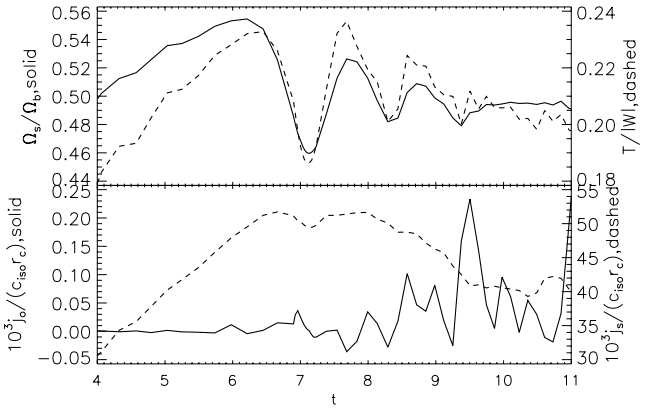

Figure 2. Evolution of stellar properties for Case 1 during the initial collapse phase. The top panel shows the spin-to-breakup frequency ratio (solid line) and the ratio of kinetic to potential energy (dashed line). The bottom panel shows the orbital angular momentum (solid line) and spin angular momentum (dashed line). Note the different scales used in the left-hand and right-hand vertical axes.

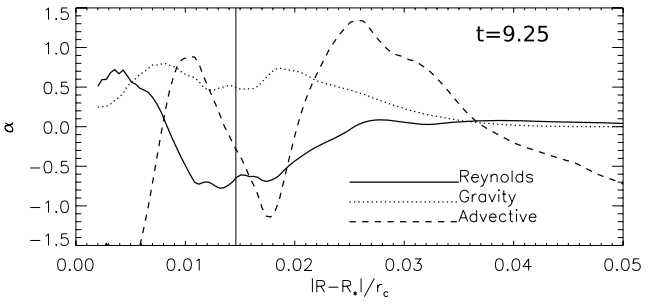

Figure 3. Case 1 early-phase spin-down: non-dimensionalized, azimuthally averaged angular momentum fluxes due to the large-scale advection, self-gravity and Reynolds stresses. $|R - R_*|$ denotes the cylindrical distance away from the star. The vertical line is $\langle r_* \rangle = 0.0146 r_c$. This snapshot corresponds to the bottom right-hand contour plot in Fig. 1.

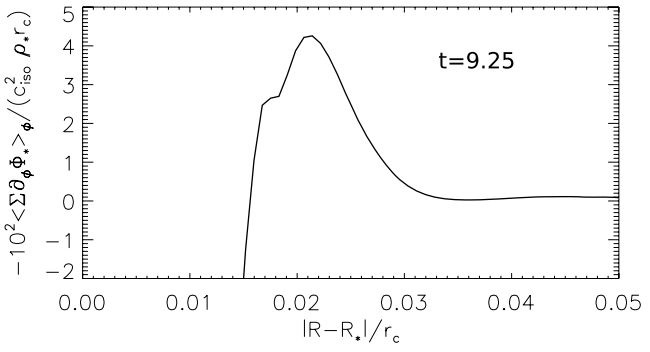

Figure 4. Case 1 early-phase spin-down. Azimuthally averaged, non-dimensionalized torque exerted by the star on its surroundings. The region $\lesssim 0.015 r_c$ corresponds to the star.

star. The $m = 1$ mode overtakes $m = 2$ at $t \sim 15$, which is when j_o begins to increase. After $t \simeq 20$, the disc forms a strong $m = 1$ asymmetry. The dominance of the $m = 1$ mode coincides with the limited evolution in stellar spin, but large amplitudes in orbital motion.

Early theoretical work shows that an $m = 1$ lopsided overdensity causes stellar orbital motion about the system's centre of mass (Adams, Ruden & Shu 1989; Heemskerk, Papaloizou & Savonije

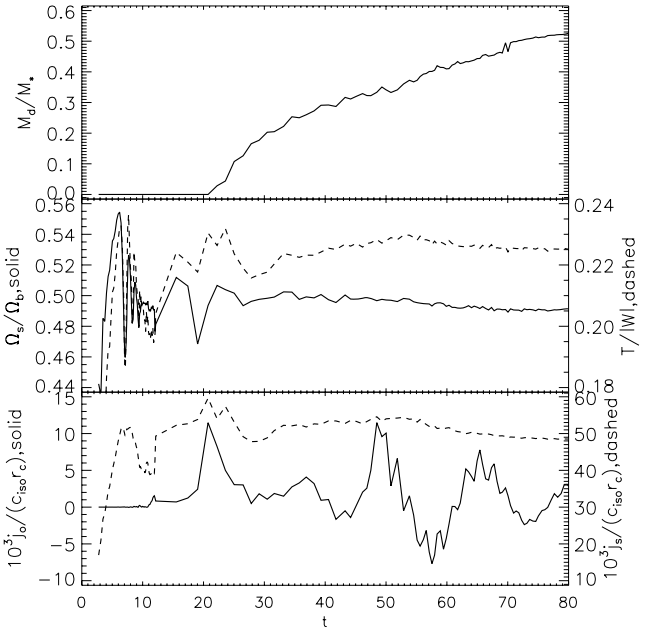

Figure 5. Case 1: evolution of the disc-to-star mass ratio (top panel) and the same stellar properties shown in Fig. 2 (middle and bottom panels) over the entire simulation. Note the different scales used for the left-hand and right-hand vertical axes.

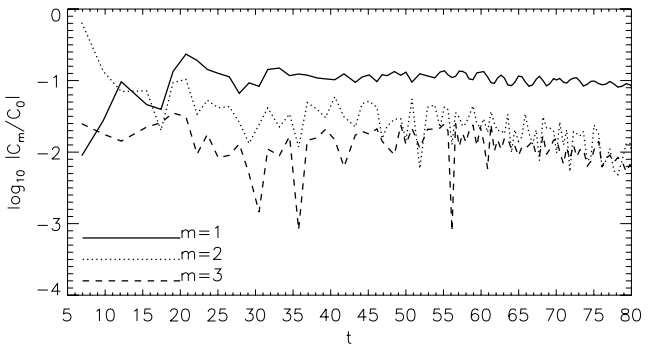

Figure 6. Case 1: evolution of non-axisymmetric modes in the surface density of a region of cylindrical radius $0.25 r_c$ and thickness $0.025 r_c$ about the star. Fourier amplitudes were integrated from a cylindrical radius of 0.02 to $0.25 r_c$ away from the star and then normalized by the axisymmetric amplitude.

1992). In those studies, the star is treated as a point mass, so star–disc torques can *only* affect the star's orbital motion. Although we model the star as a finite-sized polytrope, and thus have an associated spin angular momentum, the angular momentum exchange between the star and the $m = 1$ dominated disc is still in orbital angular momentum. Changes to the spin angular momentum are apparently inhibited.

Fig. 7 shows the evolution of the dimensionless mass-accretion rate. During the very early stages ($t \lesssim 7$), that is, the initial spin-up phase, $\xi_{sim} \sim 4$ and roughly constant (recall the initialization parameter $\xi = 5.58$). $\xi_{sim} < \xi$ since the core has angular momentum, so spherically symmetric collapse cannot occur. The sharp drop in ξ_{sim} in $7 \lesssim t \lesssim 10$ coincides with spin-down. As the star loses angular momentum to the immediate surroundings, the latter gains angular momentum, inhibiting accretion. However, once the star-on-disc torque is reduced (because the star has spun down and become more axisymmetric), material can again fall in and ξ_{sim}

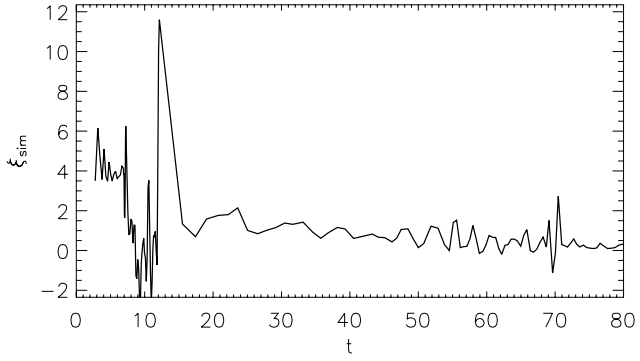

Figure 7. Case 1: non-dimensionalized mass-accretion rate. The large peak at $t \simeq 12$ may be an artefact from numerical time-derivatives.

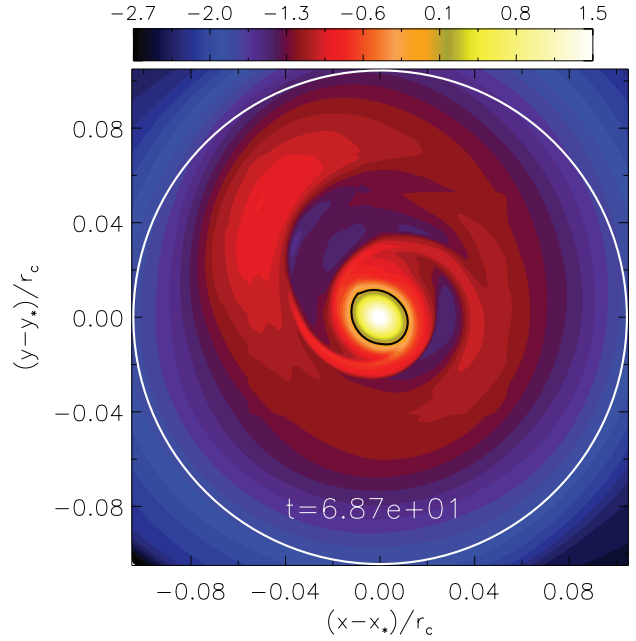

Figure 8. Case 1 towards the end of the simulation. The colour-bar indicates $\log \rho/\rho_*$ in the star's equatorial plane. The inner black line indicates $\rho = \rho_*$ and the outer white circle indicates the disc-edge R_k.

rises ($10 \lesssim t \lesssim 20$). When the stellar spin is in steady state, $\xi_{sim} < \xi$, but remains of the order of unity. The lower ξ_{sim} may result from the fact that at later times, the disc is lopsided and is not well described by accretion from a spherical cloud on to an axisymmetric disc.

4.1.3 Structure and angular momentum transport at late stages

In order to understand why spin evolution is inhibited on time-scales beyond the early phase, we analyse the disc structure, while j_s and Ω_s/Ω_b remain approximately constant. Figs 8 and 9, respectively, show the density field in real and Fourier space at $t = 68.7$. At the chosen snapshot, the star has size $\langle r_* \rangle \simeq 0.0116 r_c$ and the theoretical disc radius is $R_k \simeq 0.1 r_c$. Note that the lopsided disc is contained within R_k. We do not expect a sharp cut-off in Fourier amplitudes beyond R_k because the non-axisymmetric disc distorts the material beyond R_k.

We see that $m = 1$ dominates the outer $\simeq 40$ per cent of the disc, corresponding to the lopsided density in the contour plot. The lopsided disc behaves like a binary companion to the star, causing

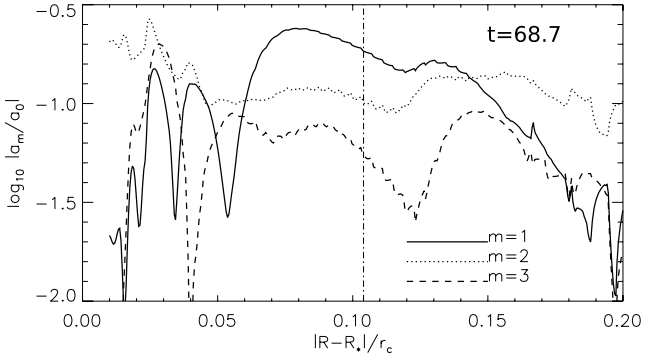

Figure 9. Case 1 towards the end of the simulation: Fourier amplitudes of non-axisymmetric modes in surface density, corresponding to the snapshot in Fig. 8. The vertical line indicates the predicted disc radius R_k.

the star to orbit about their common centre of mass. We do not expect, nor find, this motion to alter stellar spin. The fact that $m = 1$ is dominant towards the outer disc edge is favourable for inducing orbital motion because it acts like a lever arm.

Close to the star, $m = 2$ dominates, but the contour plot shows spiral arms that are thin and much less prominent than those identified during initial collapse (Fig. 1). The two arms also have different densities (reducing the amplitude of $m = 2$ symmetry). Well beyond the disc-edge R_k, $m = 2$ again dominates, but this low-density core material here is not expected to have significant impact on the stellar spin because the total mass in this region is small and because the star appears more axisymmetric as the $m = 2$ component of its potential decays with distance.

The limited spin evolution is due to ineffective gravitational coupling between the star and the disc. For a disc with m-fold symmetry, a qualitative representation of its instantaneous surface density is

$$\Sigma \sim \mathcal{A} \sin m\phi + \mathcal{B} \cos m\phi, \tag{17}$$

and for a star whose potential is dominated by k-fold symmetry, we can write

$$\Phi_* \sim \mathcal{A}_* \sin k\phi + \mathcal{B}_* \cos k\phi, \tag{18}$$

where $\mathcal{A}$, $\mathcal{B}$, $\mathcal{A}_*$ and $\mathcal{B}_*$ are real functions of radius. The instantaneous torque per unit area exerted on the disc by the star is $\mathcal{T} = -\Sigma \partial_\phi \Phi_*$. Hence, for a disc dominated by the $m = 1$ mode and a stellar potential with $k = 2$ symmetry (Fig. 8), we expect $\langle \mathcal{T} \rangle_\phi \sim 0$.

In other words, there is very little torque if the two components do not share the same symmetry ($m \neq k$). Physically, this is because there is no resonance, so for half the azimuth the torque is opposite in sign to the other half, and averages to zero. We expect a much reduced self-gravity angular momentum flux across the stellar surface in such situations.

Fig. 10 shows azimuthally averaged angular momentum fluxes for the chosen snapshot. The self-gravity flux is $\alpha_G \simeq 0.05$ near $\langle r_* \rangle$ and is an order of magnitude smaller than at $t = 9.25$ (Fig. 3), indicating ineffective gravitational spin-down. This is consistent with the limited spin evolution observed during this time and the fact that the star is much more axisymmetric than its bar-like shape at $t \lesssim 11$, thus more difficult to spin down.

We find that limited spin evolution is also correlated to significant motion of the star, induced by the $m = 1$ mode. We now examine a system with a smaller disc-to-star mass ratio and consequently less orbital motion of the star.

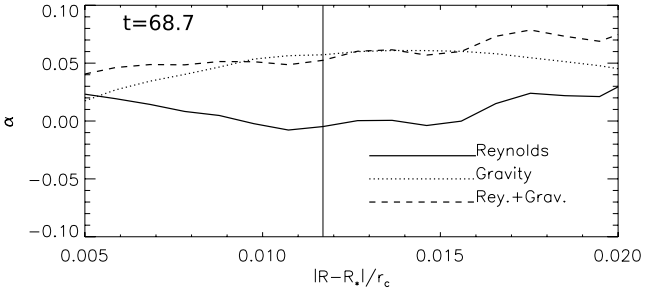

Figure 10. Case 1: non-dimensionalized, azimuthally averaged angular momentum flux towards the end of the simulation. The vertical line is $\langle r_* \rangle$. The advective flux is ~ -0.5 and beyond the scale of this plot.

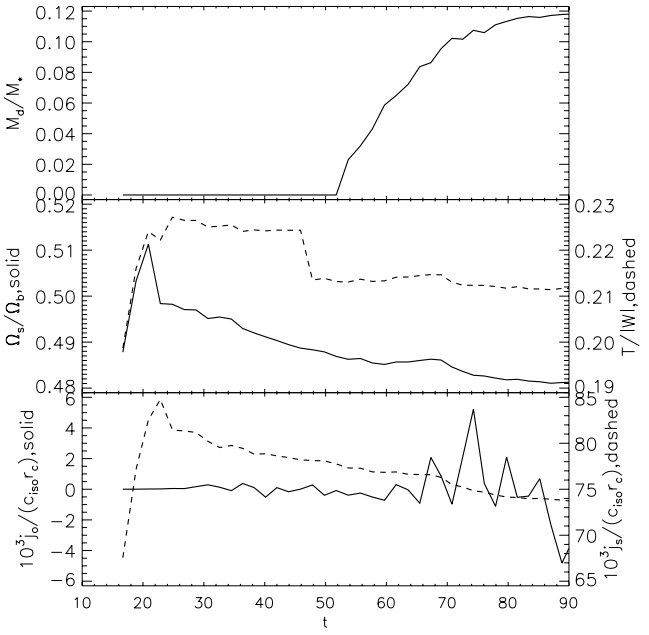

Figure 11. Case 2: evolution of the disc-to-star mass ratio (top panel), the stellar spin and kinetic-to-potential energy ratio (middle panel) and the angular momenta (bottom panel). Note the different scales used on the left-hand and right-hand vertical axes.

4.2 Case 2

This case has $m = 2$ as the dominant non-axisymmetric mode throughout the simulation. Case 2 has parameters $\xi = 2.74$ ($A = 2.8$), $h = 0.1$ and $q = 0.01$. A lower ξ corresponds to a smaller core and disc mass compared to Case 1. Increasing q corresponds to a larger star initially. Again, we wait until the star is well resolved at the finest grid level before making measurements. The star size $\langle r_* \rangle$ is typically resolved by at least 30 cells.

4.2.1 Star–disc evolution

Fig. 11 shows the evolution of disc mass and stellar properties. The phase $t \lesssim 23$ is similar to $t \lesssim 11$ of Case 1. There is an initial rapid increase in Ω_s/Ω_b, up to $\Omega_s \simeq 0.51\Omega_b$, followed by rapid spin-down, abruptly stopping at $\Omega_s \simeq 0.498\Omega_b$. However, unlike Case 1, for $t > 23$, there is a notable, almost monotonic, decrease in Ω_s/Ω_b. Note the plateau in spin frequency around $t \simeq 65$, which coincides with increase in orbital motion (see below) when the disc becomes somewhat massive ($M_d \sim 0.08M_*$). Like Case 1 though, $T/|W|$ remains fairly constant. The final spin frequency $\Omega_s \simeq 0.482\Omega_b$ is not much lower than the maximum value attained during initial collapse, but the decreasing j_s suggests that it may further spin down if the simulation were continued.

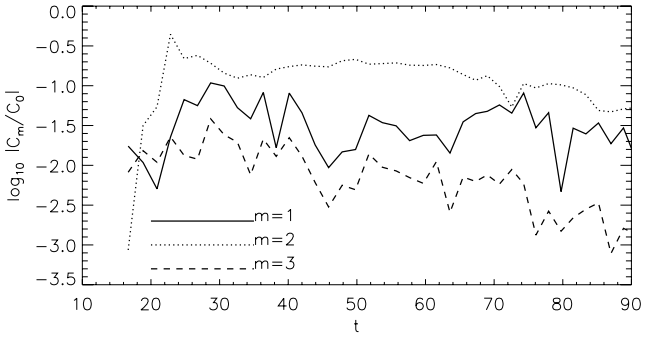

Figure 12. Evolution of non-axisymmetric modes in the surface density of the material external to the star. Fourier amplitudes were integrated over a cylindrical distance $[0.04, 0.25]r_c$ away from the star and then normalized by the axisymmetric amplitude.

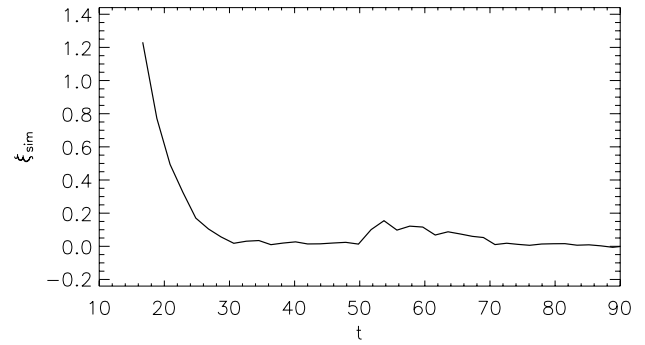

Figure 13. Case 2: the dimensionless mass-accretion rate. Note that our measurements begin after the central object is well resolved. The initial phase observed in Case 1, where ξ_{sim} is roughly constant, is not present because for this simulation, the central object is not yet well resolved during these very early times.

The evolution of the spin angular momentum is also much smoother compared to Case 1. Unlike the previous case, for $t \gtrsim 23$, j_s decreases monotonically, reaching a value $\sim$10 per cent lower than the maximum at $t \simeq 23$. Here $|j_o|$ remains at least an order of magnitude smaller than j_s, with $|j_o|$ only growing when the disc develops (the latter was also seen for Case 1).

At late times, the difference in stellar spin evolution between the present case and Case 1 is likely due to very different disc properties. In Case 2, $M_d/M_* \lesssim 0.12$, smaller than Case 1 by a factor of $\sim$4. A disc with large M_*/M_d is expected to be stable against the growth of $m = 1$ perturbations (Heemskerk et al. 1992), because there is insufficient disc mass to move the star.

Fig. 12 shows the evolution of non-axisymmetric modes in surface density and is very different from Case 1. Here, the $m = 2$ mode remains dominant throughout the simulation. This is consistent with the idea that the $m = 2$ mode provides the spin-down torque, while the $m = 1$ mode produces orbital motion.

Fig. 13 shows the measured mass-accretion rate. ξ_{sim} is smaller than Case 1 because of the lower mass core. As before, there is a drop in the accretion associated with self-limited spin. At late times, ξ_{sim} is roughly constant but is much smaller than ξ. This could be because we have a disc which is receiving angular momentum from the spin-down of the central star. This can be thought of as an accretion disc with a positive torque applied at the inner boundary

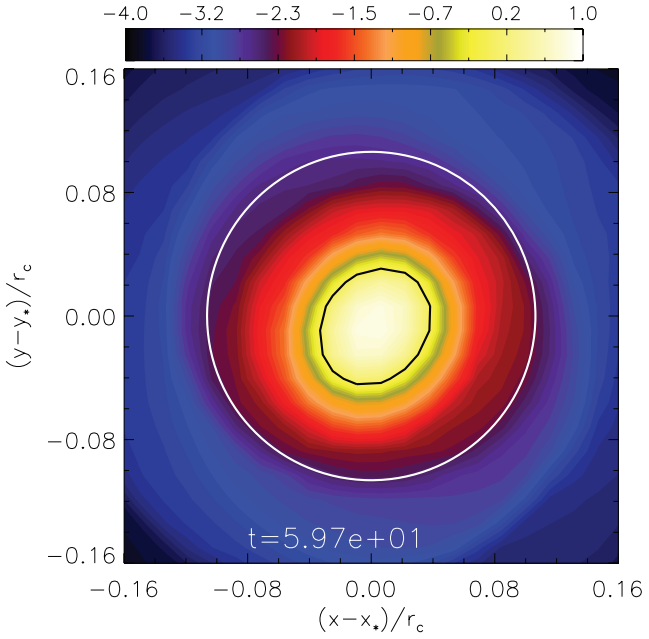

Figure 14. Case 2: snapshot of log (ρ/ρ_*) in the star's equatorial plane. The inner black line indicates $\rho = \rho_*$ and the outer white line indicates R_k.

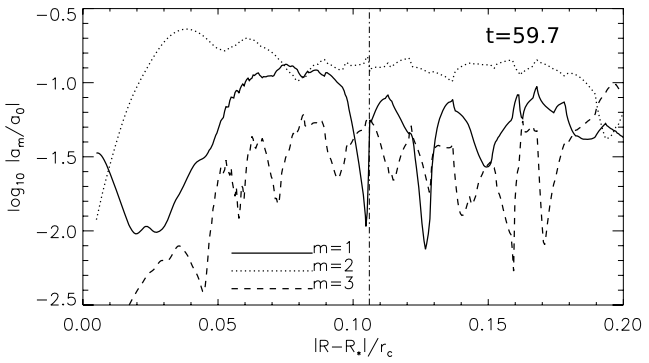

Figure 15. Case 2: Fourier amplitudes of non-axisymmetric modes in the surface density corresponding to Fig. 14. The predicted disc edge is marked by the vertical line (right-hand panel). The star has an average radius $\langle r_* \rangle \simeq 0.036 r_c$.

(Yuan & Cassen 1985). This effect is absent in Kratter et al. (2010), where ξ remains close to its initialization value, because in those simulations, the central object was represented by a sink particle that was not capable of torquing the disc.

4.2.2 *Disc structure and angular momentum flux*

We examine Case 2 at $t = 59.7$, during its long-term spin-down. Figs 14 and 15 show the density field in real and Fourier space, respectively. The average radius of the star is $\langle r_* \rangle \simeq 0.036 r_c$ and the theoretical disc edge is $R_k \simeq 0.106 r_c$. The contour plot shows that the bulk of the disc is within R_k of the star, but it distorts the region beyond it.

The contour plot clearly shows that the star–disc system has $m = 2$ symmetry. Note that the relative Fourier amplitudes are quite different from Case 1, as the $m = 1$ mode is never dominant. Instead, the $m = 2$ mode dominates most of the disc, and even the region beyond R_k.

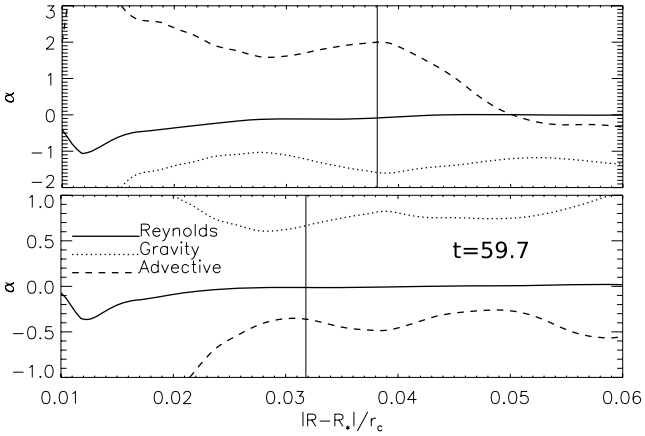

Figure 16. Case 2: non-dimensionalized angular momentum fluxes during the slow spin-down phase. Top panel: fluxes along the $\phi = \pi/4$ azimuth (approximately, the long axis of the star). Bottom panel: fluxes along $\phi = 3\pi/4$ (approximately, the short axis of the star). In each, the vertical line indicates the surface of the star along that direction. Note the different scales used for the two panels.

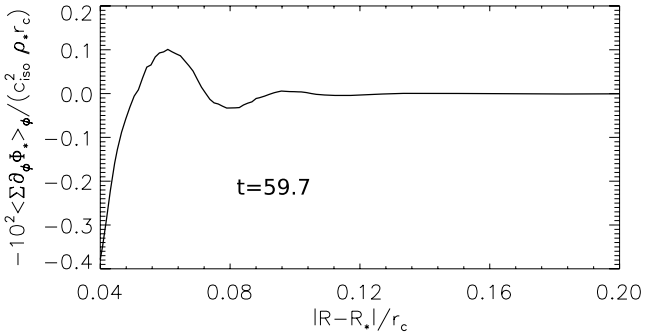

Figure 17. Case 2: azimuthally averaged torque per unit area exerted on the disc by the star, during the slow spin-down phase.

This explains why Case 2 experiences spin-down, whereas Case 1 does not. In both cases, the star has $m = 2$ symmetry, but only in Case 2 does the disc also have a significant $m = 2$ amplitude. Furthermore, the $m = 1$ amplitude in Case 2 is smaller than that of Case 1, consistent with limited orbital motion. The lack of a strong $m = 1$ mode appears favourable for spin-down via gravitational torques.

Fig. 16 shows angular momentum fluxes along the long and short axes of the star in its equatorial plane. In both cases, Reynolds stresses are negligible compared to gravity or advection. The gravity flux is large, with $\alpha_G = O(1)$. Note the sign of the fluxes depends on the azimuthal direction. Averaging the fluxes over the non-axisymmetric radius where $\rho = \rho_*$, we found $\alpha_G \sim 0.3, \alpha_R = O(10^{-3})$ and the large-scale advective flux $\alpha_A \sim -0.1$. The numerical viscosity is $\alpha_N = O(10^{-3})$. The total non-dimensional flux is $\sim$0.2, consistent with the observation of spin angular momentum loss.

We computed the potential Φ_* to find the torque exerted by the star on the surrounding disc, shown in Fig. 17. The torque becomes negative and large in amplitude towards $0.04 r_c$, or approximately the stellar surface. This large negative torque might lead to the impression that the disc is spinning up the star, contradicting the observed spin-down, but care must be taken when interpreting azimuthally averaged, one-dimensional profiles such as Fig. 17. Since the star–disc interface is non-axisymmetric, there is no single value

of the radius to represent the star–disc interface. However, the azimuthally averaged torque is positive around $0.06r_c$ from the star, which is certainly in the disc region (see Fig. 14 where this region has typical densities much lower than the transition density). This implies a net loss of spin angular momentum from the star to this disc region.

5 DISCUSSION

In our simulations, we observe an upper limit to stellar spin that is below the breakup speed. This limitation occurs during the initial spin-up of the star. This relies on the ability of the central object to deform into a non-axisymmetric shape and lose angular momentum to its surroundings by exerting gravitational torques on the external medium.

Consider a rotating, axisymmetric self-gravitating fluid body of mass M, angular momentum J and radius a in the plane perpendicular to the spin axis. We define the dimensionless angular momentum as

$$\mathcal{R} \equiv \frac{J}{\sqrt{GM^3a}}. \tag{19}$$

Now, specializing to a Maclaurin spheroid with angular momentum $J = (2/5)a^2\omega M$, where ω is the uniform spin angular frequency, the dimensionless parameter $\mathcal{R}$ for the Maclaurin spheroid is

$$\mathcal{R} = \frac{2}{5}\left(\omega \Big/ \sqrt{\frac{GM}{a^3}}\right) \equiv \mathcal{R}_{\rm Mac}. \tag{20}$$

If $\mathcal{R}_{\rm Mac} \gtrsim 0.278$, triaxial equilibrium with uniform rotation is possible (Yuan & Cassen 1985). The quantity in the square brackets is equivalent to our spin parameter Ω_s/Ω_b. If we increase $\mathcal{R}_{\rm Mac}$ from a small value, the Maclaurin spheroid will exceed the critical value above *before* it reaches the breakup speed (at which point $\mathcal{R}_{\rm Mac} = 0.4$), that is, it may become non-axisymmetric before flying apart. Obviously, our central object is not a Maclaurin spheroid, but inserting the observed maximum spin for Case 1, $\Omega_s/\Omega_b \sim 0.55$, yields $\mathcal{R}_{\rm Mac} = 0.22$, which is not too different from 0.278.

This analysis makes an important point which, together with our our simulations, suggests that the maximum stellar spin may be determined largely by the critical value of $\mathcal{R}$ (or Ω_s/Ω_b), beyond which instabilities in the rotating object produce non-axisymmetric deformations. As soon as this occurs, the object may torque the surrounding disc and lose angular momentum to it. The transition from Maclaurin spheroids to Jacobi ellipsoids (Chandrasekhar 1969) at $\mathcal{R} = 0.278$ is one example, but in general the critical value will depend on the properties of the central object, such as its EOS (Ostriker & Bodenheimer 1973). We may think of objects with lower critical values of $\mathcal{R}$ as being easier to deform and will likely be limited to smaller maximum spin rates. For example, our compressible star with smaller $\mathcal{R}_{\rm Mac}$ is easier to deform than the incompressible Maclaurin spheroid.

In our simulations, we treat the star as a simple $n = 3/2$ polytrope, but this is obviously an oversimplification of true protostellar structure, which will in general depend on its mass and evolutionary state. Even if we were to include a more realistic treatment of the EOS for stellar material, our limited resolution would make it impossible to study the star's deformation in anything but a very schematic manner. Such a study is beyond the scope of this paper, but due to this limitation we should be cautious about putting too much weight on the exact numerical values we compute for the gravitational spin-down torque. Our general conclusions that the initial spin-up is self-limited to well below breakup, and that a prominent $m = 2$ mode in the surrounding disc is capable of providing a further, long-term spin-down torque, should be robust. In particular, it is important to note that the argument we have given above is completely dimensionless and does not depend in any way on the true physical sizes of protostars or their discs.

A related issue is the degree of deformation needed for effective angular momentum exchange between the star and its surroundings. In our simulation, the density changes smoothly across the star–disc interface, whereas, in reality, the radiation from both the accretion shock and the stellar surface reduces the entropy of stellar material well below that of disc material. This causes stellar matter to be far denser than the matter in the disc immediately outside the star, an effect that we miss because our simulations are non-radiative. A larger density contrast would make the star's gravitational field stronger and would therefore increase the effectiveness of gravitational angular momentum transport relative to that in our simulations. As a result, real stars probably spin down more effectively than we have found and require less non-axisymmetry to achieve the same torque (cf. Yuan & Cassen 1985). Thus, a more realistic treatment of stellar structure may actually strengthen the effect we have identified.

5.1 Numerical issues

The issue of numerical viscosity was not discussed in detail, which could be important for numerical studies of rotating fluids in a Cartesian box. Angular momentum conservation can be violated near the centre of the rotating fluid. However, we have recalculated spin angular momenta excluding the innermost few cells and found negligible effect on their evolution. In addition, lower resolution runs were performed which yield similar angular momentum evolution. We are thus confident that the observed correlation between spin evolution and the evolution of disc modes is a physical result.

We have focused on only two simulation runs. Although insufficient to predict stellar spin evolution as a function of the problem parameters, our results provide a useful guide to future numerical studies. We expect discs that develop prominent global $m = 2$ spirals to be most effective at spinning down the star through gravitational torques, because the star will usually have the same symmetry.

5.2 Additional caveats

It should be noted that the physics in our problem setup are highly simplified. The dynamical range covered in our simulations does not correspond to an entire, realistic star–disc system. This discrepancy could potentially limit the applicability of our results to realistic star–disc systems.

One issue is that if the star-on-disc torque is most significantly close to the stellar surface, then such torques will be ineffective if there exists a significant gap between the star and the inner disc edge. A gap may be caused by magnetic fields for low-mass stars. However, using the model of Matt & Pudritz (2005), one finds that for massive stars the truncation radius is actually inside the star, implying no gap (Rosen, Krumholz & Ramirez-Ruiz, in preparation). Gravitational torques may then play a role. In addition, if gravitational torques are a result of a high protostar spin rate, which enables triaxiality, then material must have fallen on to the star, adding to its angular momentum in the first place. The smooth star–disc boundary in our simulations is then self-consistent with limiting spin via gravitational torques in the early stages of collapse.

Finally, although we have demonstrated the existence of star–disc torques, we caution that the exact magnitudes of the torques will likely depend on the structure of the disc, which can in turn

be modified by magnetic fields and radiation. We have not included these effects, and in their presence, the true spins of stars undergoing gravitational torque-regulated spin-up as they form will likely be quantitatively different from what we have found, but our general conclusions should hold.

6 CONCLUSIONS

We performed hydrodynamic simulations of the collapse of an isothermal cloud leading to the formation of a disc with a dense central object. We focused on the evolution of the central object's spin and its relation to disc properties.

We find that the initial spin-up of the central object does not exceed ∼50 per cent of its breakup speed because increasing spin also increases its deformation into a bar-like object (possibly through an instability), on which the external material exerts a negative torque. Spin-down occurs over a period that is short compared to star formation time-scales.

We also find that when the surrounding disc develops a dominant $m = 1$ disturbance, the central object's spin evolution is inhibited, and large orbital motions are induced by the disc. Our experiments suggest, perhaps counter-intuitively, that massive discs are less able to provide long-term gravitational spin-down torques on a star because such discs are prone to developing $m = 1$ lopsided modes.

Although spin-down was observed over the simulation time-scale for systems with $m = 2$ symmetry, the spin-down rate is small compared to that during the earliest phase of collapse. The precise value of this upper limit may depend on the internal structure of the central object in ways that we have not explored. In general, we expect that structures that are easier to deform, in the sense that a smaller spin-to-breakup frequency ratio is needed to allow non-axisymmetry, will yield smaller maximum spin rates than structures that require larger spin-to-breakup frequencies to become non-axisymmetric.

An upper limit to the spin rate has important implications for stellar evolution. Strong rotational mixing may occur for large spin rates and allow the star to bypass the red giant phase (Yoon & Langer 2005; Woosley & Heger 2006). The critical spin rate found by Woosley & Heger is ≃40 per cent of breakup. As another example, Ekström et al. (2008) found that high rotation (≃40–70 per cent breakup) can increase metal production in initially metal-free stars. However, if gravitational torques limit stellar spin to ≃50 per cent of breakup, strong rotational mixing or increased metal production may be difficult to achieve because once the star reaches the main sequence, stellar winds provide further spin-down. A maximum stellar spin set by gravitational torques can be used to constrain the parameter space for stellar evolution calculations.

ACKNOWLEDGMENTS

This project was initiated during the ISIMA 2010 summer programme, funded by the NSF CAREER grant 0847477, the France-Berkeley fund, the Institute for Geophysics and Planetary Physics and the Center for Origin, Dynamics and Evolution of Planets. We thank them for their support. M-KL acknowledges support from the Isaac Newton Trust and St. John's College, Cambridge. MRK acknowledges support from an Alfred P. Sloan Fellowship, NSF grants AST-0807739 and CAREER-0955300, and NASA through Astrophysics Theory and Fundamental Physics grant NNX09AK31G and a Spitzer Space Telescope Theoretical Research Program grant. KMK is supported by an Institute for Theory and Computation Postdoctoral Fellowship at Harvard College Observatory.

REFERENCES

Adams F. C., Ruden S. P., Shu F. H., 1989, ApJ, 347, 959
Bate M. R., 1998, ApJ, 508, L95
Bisnovatyi-Kogan G. S., 1993, A&A, 274, 796
Bodenheimer P., 1995, ARA&A, 33, 199
Chandrasekhar S., 1969, Ellipsoidal Figures of Equilibrium. Yale Univ. Press, New Haven
Eisner J. A. et al., 2010, ApJ, 718, 774
Ekström S., Meynet G., Chiappini C., Hirschi R., Maeder A., 2008, A&A, 489, 685
Federrath C., Sur S., Schleicher D. R. G., Banerjee R., Klessen R. S., 2011, ApJ, 731, 62
Fisher R. T., 2002, PhD thesis, Univ. California, Berkeley
Fisher R. T., 2004, ApJ, 600, 769
Glatzel W., Obach C., 1999, MNRAS, 308, 147
Goodman A. A., Benson P. J., Fuller G. A., Myers P. C., 1993, ApJ, 406, 528
Heemskerk M. H. M., Papaloizou J. C., Savonije G. J., 1992, A&A, 260, 161
Hennebelle P., Commerçon B., Joos M., Klessen R. S., Krumholz M., Tan J. C., Teyssier R., 2011, A&A, 528, A72
Jappsen A., Klessen R. S., 2004, A&A, 423, 1
Klein R. I., 1999, J. Comput. Appl. Math., 109, 123
Kratter K. M., Matzner C. D., 2006, MNRAS, 373, 1563
Kratter K. M., Matzner C. D., Krumholz M. R., 2008, ApJ, 681, 375
Kratter K. M., Matzner C. D., Krumholz M. R., Klein R. I., 2010, ApJ, 708, 1585
Krumholz M. R., McKee C. F., Klein R. I., 2004, ApJ, 611, 399
Krumholz M. R., Klein R. I., McKee C. F., 2007, ApJ, 656, 959
Krumholz M. R., Klein R. I., McKee C. F., Offner S. S. R., Cunningham A. J., 2009, Sci, 323, 754
Lynden Bell D., Kalnajs A. J., 1972, MNRAS, 157, 1
Masunaga H., Miyama S. M., Inutsuka S., 1998, ApJ, 495, 346
Matt S., Pudritz R. E., 2005, MNRAS, 356, 167
Matt S., Pudritz R., 2008, in van Belle G., ed., ASP Conf. Ser. Vol. 384, Understanding the Spins of Young Stars. Astron. Soc. Pac., San Francisco, p. 339
Matt S. P., Pinzón G., de la Reza R., Greene T. P., 2010, ApJ, 714, 989
Offner S. S. R., Kratter K. M., Matzner C. D., Krumholz M. R., Klein R. I., 2010, ApJ, 725, 1485
Ostriker J. P., Bodenheimer P., 1973, ApJ, 180, 171
Peters T., Klessen R. S., Mac Low M., Banerjee R., 2010, ApJ, 725, 134
Peters T., Banerjee R., Klessen R. S., Mac Low M., 2011, ApJ, 729, 72
Popham R., Narayan R., 1991, ApJ, 370, 604
Saigo K., Tomisaka K., 2006, ApJ, 645, 381
Saigo K., Tomisaka K., 2011, ApJ, 728, 78
Saigo K., Tomisaka K., Matsumoto T., 2008, 674, 997
Schleicher D. R. G., Sur S., Banerjee R., Klessen R. S., Federrath C., Arshakian T., Beck R., Spaans M., 2011, Cosmic Radiation Fields: Sources in the Early Universe, preprint (arXiv:1102.3558)
Shakura N. I., Sunyaev R. A., 1973, A&A, 24, 337
Shu F. H., 1977, ApJ, 214, 488
Stacy A., Bromm V., Loeb A., 2011, MNRAS, 413, 543
Tan J. C., McKee C. F., 2004, ApJ, 603, 383
Truelove J. K., Klein R. I., McKee C. F., Holliman II J. H., Howell L. H., Greenough J. A., Woods D. T., 1998, ApJ, 495, 821
Wolff S. C., Strom S. E., Dror D., Lanz L., Venn K., 2006, AJ, 132, 749
Woosley S. E., Heger A., 2006, ApJ, 637, 914
Yoon S., Langer N., 2005, A&A, 443, 643
Yuan C., Cassen P., 1985, Icarus, 64, 435

This paper has been typeset from a TEX/LATEX file prepared by the author.